Self-healing capability of novel eco-epoxy adhesives based on the modified tannic acid on Al adherends tested in a single lap joint

Tomić, Nataša Z.; Saleh, Mohamed Nasr; Saeedifar, Milad; Marinković, Aleksandar; Freitas, Sofia Teixeira de

DOI
10.1016/j.ijadhadh.2021.103013

Publication date
2021

Document Version
Final published version

Published in
International Journal of Adhesion and Adhesives

Aerospace Science and Technology 125 (2022) 107086

Contents lists available at ScienceDirect

Aerospace Science and Technology

www.elsevier.com/locate/aescte

Performance and noise prediction of low-Reynolds number propellers using the Lattice-Boltzmann method

Gianluca Romani *, Edoardo Grande, Francesco Avallone, Daniele Ragni, Damiano Casalino

Delft University of Technology, Kluyverweg 1, 2629HS, Delft, the Netherlands

ARTICLE INFO

Article history:
Received 20 May 2021
Received in revised form 6 August 2021
Accepted 30 August 2021
Available online 6 September 2021
Communicated by Damiano Casalino

Keywords:
Lattice-Boltzmann method
Propeller
Low-Reynolds number
Aerodynamics
Aeroacoustics

ABSTRACT

This paper proposes a CFD/CAA-based approach to predict the aerodynamic performances and tonal/broadband noise radiation of low-Reynolds number propellers at engineering level. Broadband self-noise prediction of low-Reynolds number propellers is particularly challenging, due to the requirement for the employed computational method to emulate the complexity of the laminar/turbulent boundary-layer behavior on the blade. In this study, the numerical flow solution is obtained by using the Lattice-Boltzmann/Very Large Eddy Simulation method, whereas far-field noise is computed through the Ffowcs-Williams & Hawkings' acoustic analogy applied on the propeller surface. A zig-zag transition trip on the propeller blades is used in the numerical setup to reproduce resolved turbulent pressure fluctuations in boundary-layer for broadband noise computation at a relatively low computational cost. The effect of using a transition trip to simulate low-Reynolds number propellers, as well as the impact of its chordwise position on the calculation of performances and radiated noise, is outlined. The trip position marginally affects the thrust and to a slightly larger extent the torque prediction. Tonal noise at the blade-passing frequencies does not show a relevant sensitivity to it, whereas broadband noise is found to be slightly more influenced by the chordwise position of the trip, especially at high advance ratios. The low sensitivity of the numerical results to the trip location, as well as their good agreement with loads and noise measurements carried out in the A-Tunnel of TU-Delft, demonstrates the robustness of the proposed approach for industrial applications.

1. Introduction

In recent years, the aeroacoustics associated to low-Reynolds number ($Re_c < 1 \cdot 10^5$ based on the chord at 75% of the blade radius) propellers has significantly gained the attention in the aerospace community [1–5], due to the rapid expansion of small rotary-wing UAVs for commercial, scientific or recreational applications, as well as to the emergent market of propeller-driven PAVs for on-demand urban air transport [6]. Since these are full-electric and battery-powered vehicles that are expected to operate in densely populated areas, high propulsive efficiency and low-acoustic footprint represent essential target of their design process, with the aim of increasing endurance and limiting noise nuisance towards the community [6].

Due to the lower blade tip velocity of small-scale propellers compared to traditional helicopter rotors, broadband self-noise, in the form of turbulent boundary-layer trailing-edge noise, becomes a relevant contributor to the far-field acoustics in addition to steady/unsteady loading and thickness noise [7]. Turbulent boundary-layer trailing-edge noise is associated to the scattering of the hydrodynamic pressure fluctuations, within the turbulent boundary-layer developing over the blade surface, when they pass a geometrical singularity such as a sharp trailing-edge [8]. Moreover, the performance and noise signature of propellers operating at low-Reynolds numbers can be significantly affected by the behavior of the boundary-layer developing over the blades. In the low-Reynolds number regime, the boundary-layer remains laminar for a relatively large extension of the blade chord and possibly separates. The resulting separated shear layer, depending on the local angle of attack, Reynolds number, airfoil characteristics and incoming flow conditions, can reattach as either a laminar or turbulent boundary-layer and lead to the formation of a laminar separation bubble [9,10]. The position and length of the laminar separation bubble are mainly influenced by the local airfoil angle of attack and Reynolds number [9], and can have a detrimental impact on both propeller performances [11] and noise emissions [12].

The presence of a laminar separation bubble can significantly alter the airfoil pressure distribution, resulting in an increment of

* Corresponding author.
E-mail address: g.romani@tudelft.nl (G. Romani).

https://doi.org/10.1016/j.ast.2021.107086

Nomenclature

c	Airfoil chord ..... m	V_{rms}	Flow velocity root-mean-square ..... m/s
c_∞	Free-stream speed of sound ..... m/s	x, y, z	Airfoil reference frame coordinates ..... m
C_p	Pressure coefficient ..... -	x_b, y_b, z_b	Blade reference frame coordinates ..... m
C_Q	Propeller torque coefficient ..... -	x_f, y_f, z_f	Freestream reference frame coordinates ..... m
C_T	Propeller thrust coefficient ..... -	$y+$	Non-dimensional wall-distance in viscous units .. -
D	Propeller diameter ..... m	η	Propeller propulsive efficiency ..... -
f	Frequency ..... Hz	ν	Flow kinematic viscosity ..... m^2/s
J	Advance ratio ..... -	ρ_∞	Free-stream density ..... kg/m^3
k	Critical trip height ..... m	Φ_{aa}	Far-field noise power spectral density ..... dB/Hz
$L_{p(1/3)}$	Far-field noise 1/3-octave sound pressure level dB	Φ_{pp}	Wall-pressure power spectral density ..... dB/Hz
M	Mach number ..... -	ω	Propeller angular velocity ..... RPM
n	Revolution per second ..... RPS	BEMT	Blade Element Momentum Theory
p_∞	Free-stream static pressure ..... Pa	BPF	Blade Passing Frequency
Q	Propeller torque ..... Nm	CAA	Computational Aero-Acoustics
r	Propeller radial coordinate ..... m	CFD	Computational Fluid Dynamics
R	Propeller radius ..... m	DES	Detached Eddy Simulation
Re_c	Chord-based Reynolds number ..... -	FW-H	Ffowcs Williams & Hawkings
Re_k	Critical roughness height-based Reynolds number -	LBM	Lattice-Boltzmann Method
T	Propeller thrust ..... N	LES	Large Eddy Simulation
T_∞	Free-stream temperature ..... K	LRF	Local Reference Frame
V_∞	Free-stream axial velocity magnitude ..... m/s	PAV	Personal Aerial Vehicle
V_r	Flow velocity magnitude in the blade reference frame ..... m/s	RANS	Reynolds-Averaged Navier-Stokes
		UAV	Unmanned Aerial Vehicle
V_{r_∞}	Free-stream velocity magnitude in the blade reference frame ..... m/s	VLES	Very Large Eddy Simulation
		VR	Variable Resolution

the drag generated by the local blade section [13]. Furthermore, a feedback loop between hydrodynamic instability waves in the boundary-layer and acoustic waves, associated to the scattering of such instabilities at the trailing-edge, can lead to a significant noise increment when the laminar separation bubble is sufficiently close to the trailing-edge [14], with narrowband tones over a broadband hump featuring the corresponding far-field noise spectrum for 2D airfoils [15]. Concerning rotor applications, a high frequency broadband hump has been reported in the far-field noise spectrum in the presence of a laminar separation bubble on the blade surface in previous experimental studies, with [14] and without [12,14,16] the emergence of a strong tonal content strictly ascribable to the acoustic feedback loop. The presence of a broadband hump with no tonal contribution was associated to the mere trailing-edge scattering of instability waves without the occurrence of a proper acoustic feedback [14].

The accurate prediction of low-Reynolds number propellers aerodynamics aeroacoustics is a quite challenging topic from a computational perspective. Low-fidelity approaches such as BEMT-2D viscous panel methods for propeller loadings computation (in which 2D viscous panel method computations are used to provide the sectional force coefficients for the BEMT calculation) [16] coupled with compact monopole/dipole FW-H formulations for far-field noise radiation [17], can provide very good forces prediction [16], as well as tonal noise estimation within 2-5 dB accuracy [2,16], at a negligible computational cost. However, the accuracy of such approaches is limited as far as turbulent boundary-layer trailing-edge noise prediction is also concerned, due to the relatively low predictive capability of the semi-empirical wall-pressure spectrum models, which are often used in their semi-analytical trailing-edge noise models [7,16]. A recent benchmark study on a small-scale propeller aeroacoustics conducted by Casalino et al. [16] showed a large sensitivity of broadband noise to the particular wall-pressure spectrum model employed, with a scatter of broadband noise predictions within 30 dB among the different models.

Higher fidelity scale-resolving methods, such as DES [18], hybrid RANS-LES [18] or LBM-VLES [19,20], represent more accurate approaches to compute both tonal and broadband rotor/propeller noise at computational cost that is lower than that required by LES and complies with industrial turnaround times. Nevertheless, these global hybrid CFD methods may suffer in accurately predicting flows characterized by shallow regions of boundary-layer separation and re-attachment [21]. Moreover, they typically rely on the presence of a sufficiently high level of flow instabilities in the numerical solution to switch from modeled to scale-resolving turbulence mode, and thus to generate an unsteady resolved turbulent content [22], which is essential for the sake of turbulent boundary-layer trailing-edge noise prediction. Such shortcomings make capturing laminar separation bubbles and laminar-to-turbulent boundary-layer transition, as well as the associated trailing-edge noise radiation, quite challenging problems to be addressed with these hybrid CFD methods.

In this study, the commercial CFD/CAA solver SIMULIA Power FLOW®, based on a Lattice-Boltzmann Method hybridized with a Very Large Eddy Simulation (LBM-VLES) model for turbulence, is employed with a computational approach to emulate the flow complexity of low-Reynolds number propellers and predict the resulting far-field noise radiation. The aerodynamic noise generated by the propeller is evaluated by using an acoustic analogy based on Farassat's formulation 1A of the Ffowcs Williams & Hawkings' (FW-H) equation applied to the propeller surface. Similarly to DES or global hybrid RANS-LES approaches, the LB-VLES method used in this work relies on the presence of some instabilities in the numerical flow solution to force the VLES turbulence model to enter into the scale-resolving mode. This paper proposes a computational approach based on the usage of a low-intrusive zig-zag transition trip to address this aspect. The zig-zag trip constitutes a geometric imperfection on the blade surface that guides the VLES turbulence model towards a scale-resolving mode and triggers the formation of vortical structures, with scales able to emulate the complexity of the low-Reynolds boundary-layer on the blade, which is required

for turbulent boundary-layer trailing-edge noise computation. The validation of such an approach is accomplished by comparison with forces and noise measurements carried out in the A-Tunnel of TU-Delft. Two different tripping approaches are considered by placing the trip arbitrarily on the quarter-chord line of the blade, and along the expected turbulent boundary-layer transition line, as predicted by a BEMT code coupled with a 2D viscous panel method. With this regard, this paper is aimed at: (i) assessing the proposed computational approach to predict the performances and noise radiation associated to low-Reynolds number propellers; (ii) analyzing the impact and limitations of using a transition trip for low-Reynolds number propeller simulation, as well as to investigate the effect of the trip line location on the propeller loads and noise radiation.

The paper is organized as follows. Section 2 briefly introduces the computational methodology adopted in this study. The propeller geometry, operating conditions and computational setup are described in Sec. 3. The numerical results are presented and discussed in Sec. 4. Finally, the main conclusions of this work are summarized in Sec. 5.

2. Computational method

The CFD/CAA solver SIMULIA PowerFLOW® 6-2019 is used in this study to compute the flow around the propeller and extract the resulting noise signature. It is based on the Lattice-Boltzmann Method (LBM) with a wall-modeled Very Large Eddy Simulation (VLES) approach used for turbulence modeling [23–30]. PowerFLOW® solves the Boltzmann equation for the distribution function $f(\mathbf{x}, t, \mathbf{v})$, which represents the probability to find, in the elementary volume d$\mathbf{x}$ around the spatial position $\mathbf{x}$ and in the infinitesimal time interval $(t, t + \mathrm{d}t)$, a number of fluid particles with velocity in the interval $(\mathbf{v}, \mathbf{v} + \mathrm{d}\mathbf{v})$. The Boltzmann equation is solved by discretizing the space velocity domain into a prescribed number of values in magnitude and direction. For low-subsonic flow simulations, the D3Q19 model is used, which employs 19 velocity states in the 3 spatial dimensions [31]. The collision operator is modeled with the Bhatnagar-Gross-Krook (BGK) approximation [31,32].

The LBM scheme is solved on a Cartesian grid composed of cubic volumetric elements (Voxels). The surface of solid bodies is discretized within each voxel intersecting the wall geometry using planar surface elements (Surfels). A boundary scheme based on a particle bounce-back process and a specular reflection process is used to reproduce no-slip and slip wall boundary condition [33], respectively. Hydrodynamic flow quantities, such as flow density and velocity, can be determined through discrete integration of the discrete distribution function [25], whereas all the other physical quantities can be determined through ideal gas thermodynamics. For simulations of rotating geometries, the computational domain is decomposed into an outer ground-fixed reference frame and an inner body-fixed Local Reference Frame (LRF). The latter is characterized by a mesh which rigidly rotates with the rotating geometry so that no relative motion between the LRF grid and the enclosed geometry occurs. An external body force term, corresponding to the inertial force introduced by the non-inertial rotating LRF, is introduced at the right hand side of the discrete Boltzmann equation for the fluid region inside the LRF domain [34]. A closed transparent interface is used between the inner and outer domains in order to connect the two fluid flow regions [35].

In this study, a hybrid CFD/CAA approach is adopted to compute the far-field noise to avoid expensive computations associated to the necessity of accurately resolving the acoustic waves propagation up to the far-field. An impermeable Ffowcs-Williams and Hawkings' (FW-H) acoustic analogy [36] is used to compute the far-field noise from the body geometry, kinematics and pressure distribution. The FW-H solver used in this work is part of the post-processing software SIMULIA PowerACOUSTICS® and is based on a forward-time solution [37] of Farassat's formulation 1A [38]. This FW-H formulation includes distributions of acoustic monopoles and dipoles (i.e. surface integrals), which are typically referred to as thickness and loading terms, while neglects the quadrupole term (i.e. volume integral), which accounts for all the possible non-linear effects in the volume surrounding the integration surface (i.e. shock waves, turbulence mixing and non-linear propagation effects). This last source term can be neglected for propellers operating at low blade-tip Mach number [8]. In such operating conditions, no shock waves occur on the propeller blades and dipole noise sources, such as broadband trailing-edge noise and harmonic loading noise, which respectively scale as the fifth [39] and sixth [40] powers of the Mach number, are significantly more efficient than the quadrupoles in the turbulent wake of the propeller, which scale with the eighth power of the Mach number [41].

3. Propeller geometry and computational setup

The geometry used in this study (shown in Fig. 1(a)) is a two-bladed propeller designed at TU-Delft and derived from an APC 9x6 propeller. It is characterized by a radius R of 0.15 m and NACA 4412 airfoil sections, which are merged with the propeller hub by elliptical sections (for $r < 0.01$ m). The airfoil chord and twist spanwise distributions are shown Fig. 1(b). The propeller hub radius is 1.25 cm and connected to a nacelle of 5 cm diameter and 52 cm length. The propeller geometry under examination has been experimentally tested in the A-Tunnel of TU-Delft and will be used for future low-Reynolds number propeller benchmarking. A more detailed description of the propeller geometry and experiment that is used as benchmark in this work can be found in Refs. [16,42]. Fig. 1(a) shows the free-stream (x_f, y_f, z_f) and blade coordinate (x_b, y_b, z_b) systems that are used in this study. The former is rigidly connected to a ground-fixed reference frame, whereas the latter rigidly rotates with the blade geometry. The free-stream velocity V_∞ is directed along the x-axis of the free-stream coordinate system. The propeller is operated at fixed angular velocity ($\omega = 5000$ RPM) and five different advance ratios $J = 0.0, 0.24, 0.4, 0.6, 0.8$ (where $J = V_\infty/(nD)$, with n denoting the revolutions per second and D the propeller diameter), by varying the free-stream velocity from 0 to 20 m/s. The resulting tip Mach number is 0.23 and the Reynolds number based on the local airfoil chord and velocity ranges between $5 \cdot 10^4$ and $1 \cdot 10^5$ across the different section and axial velocity conditions. The free-stream static pressure and temperature considered are $p_\infty = 99000$ Pa and $T_\infty = 293.15$ K, respectively.

Fig. 2(a) depicts the computational setup used in this study. The computational fluid domain is a spherical volume of $325D$ radius centered around the propeller. Free-stream static pressure and velocity, and turbulence intensity of 0.1% of the free-stream velocity are prescribed on its outer boundary. The experimental wind tunnel geometry is not modeled in the computational setup. An acoustic sponge is used to dissipate the out-going acoustic waves and minimize the backward reflection from the outer boundary and reproduce a full anechoic digital environment. The acoustic sponge is defined by two concentric spheres of radius $15D$ and $55D$, respectively, centered around the propeller. The fluid kinematic viscosity is gradually increased starting from its physical value within the inner sphere, up to an artificial value two orders of magnitude higher outside the outer one. The acoustic sponge, which has no aerodynamic effect in the flow region of interest, is placed based on previous LBM/VLES benchmark and validation studies carried out by the authors [16,19].

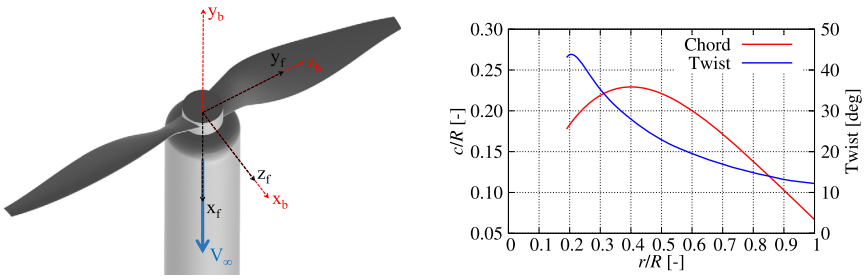

(a) *Propeller and coordinate systems* (b) *Airfoil chord and twist distributions*

Fig. 1. Propeller geometry, coordinate systems, airfoil chord and twist spanwise distributions. (For interpretation of the colors in the figure(s), the reader is referred to the web version of this article.)

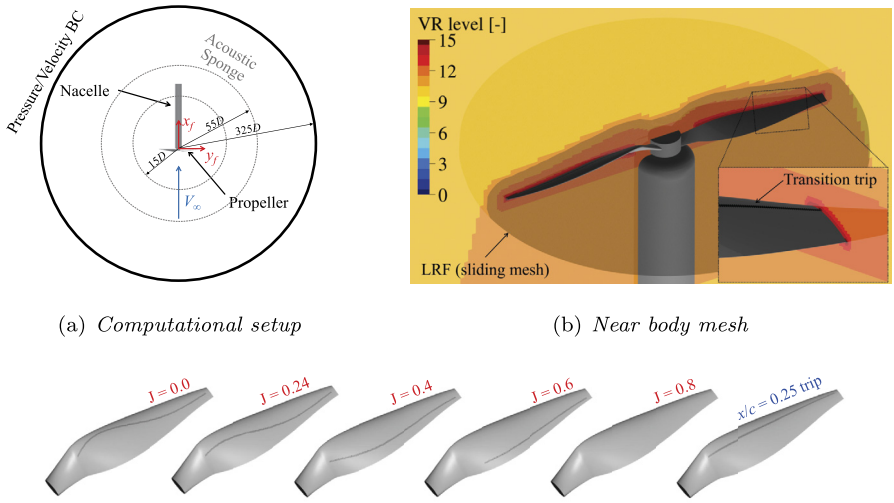

(a) *Computational setup* (b) *Near body mesh*

(c) *Trip line distributions: Opty∂B-*BEMT *trips (red) and* $x/c = 0.25$ *trip (blue)*

Fig. 2. Sketch of (a) computational setup (not drawn to scale), (b) near body mesh and (c) trip line distributions on the blade suction side.

Since one of the goals of the present study is to predict trailing-edge noise of low-Reynolds number propellers with turnaround times feasible for industrial applications, it is necessary to resolve part of the energy spectrum associated to the turbulent pressure fluctuations in the simulated boundary-layer. Hence, a zig-zag transition trip of 0.17 mm thickness, 0.9 mm amplitude and wavelength is used on the suction side of the blade for $r/R > 0.2$ to drive the LBM-VLES scheme from turbulence modeling to scale-resolving behavior and trigger the formation of vortical structures, with scales capable of emulating the complexity of a low-Reynolds number boundary-layer at a relatively low computational cost. The zig-zag topology is preferred to other trip shapes due to its high efficiency and low critical roughness height-based Reynolds number in initiating transition [43]. The height of 0.17 mm, corresponding to three finest voxels, is selected to ensure that the flow volume surrounding the trip is sufficiently fine discretized, according to the employed computational mesh, and that the trip is able to initiate transition regardless its chordwise position for the sake of industrial robustness. Indeed, the blade suction side is tripped considering two different strategies: (i) trip line arbitrary positioned at 25% of the chord; (ii) trip distributed along the expected boundary-layer transition line (i.e. at the end of the laminar separation bubble) as predicted by *Opty∂B-*BEMT, a BEMT code coupled with a 2D viscous panel method developed by Dassault Systèmes. The former is a modeling choice that might be followed in absence of any information on the boundary-layer transition process, while the latter represents an approach more consistent with the physics of the problem, according to which transition is likely to occur across the laminar separation bubble reattachment line. For both cases, no trip is placed on the blade pressure side, since no laminar-to-turbulent boundary layer transition is expected to occur by the BEMT/viscous panel method code. Fig. 2(c) shows the trip line positions predicted by the BEMT model for the different advance ratios considered, as well as the configuration with trip located at 25% of the blade chord. Portions of the trip line exceeding 80% of the chord were omitted from the generation of the zig-zag trip to avoid placing the trip excessively close to the blade trailing-edge and promoting an undesired flow separation.

Fig. 2(b) shows the details of the computational setup and mesh in proximity of the propeller geometry. The propeller and hub are encompassed by a volume of revolution that defines the Local Reference Frame (LRF), namely the rotating sliding mesh domain used to reproduce the propeller rotation. The solid FW-H integration surface used to compute the far-field noise radiation coincides with the propeller, hub and nacelle surfaces. A total of 16 Variable Resolution (VR) regions are used to discretize the whole fluid domain, with the finest resolution level (VR15) placed around the blade trip and trailing-edge. A resolution of 200 voxels along the mean chord (22.85 mm) is used in the second finest resolution level (VR14), resulting in a smallest voxel size of 0.06 mm, a mean $y+ \approx 5$ on the blade surface and an overall mesh size of 107 million voxels. The computational cost is 840 CPUh/rev on a 430 cores

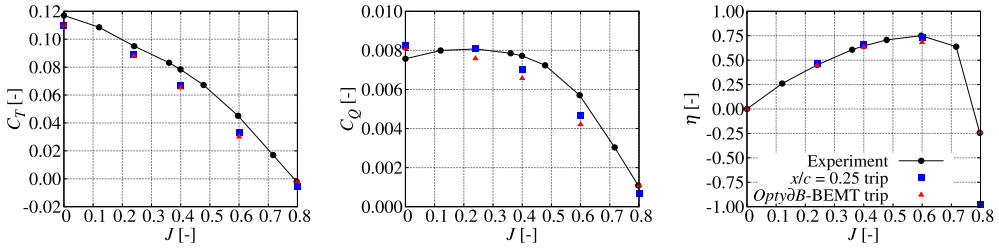

Fig. 3. Thrust (left), torque (center) and propulsive efficiency (right) coefficients at different advance ratios ranging between $J = 0.0$ and $J = 0.8$. Comparison between measurements and numerical solutions obtained with the $x/c = 0.25$ and *Opty∂B*-BEMT trips.

cluster with Intel Xeon CPU E5-2697 2.6 GHz. The whole fluid domain is initialized with the instantaneous flow solution from a statistically converged coarser simulation. Hence, after a settling time corresponding to 2 propeller revolutions, the sampling of relevant flow data is started for 10 additional revolutions. Acoustic data is sampled at 365 kHz with spatial averaging of 0.5 mm on the solid FW-H integration surface. Fourier transformed data is obtained with 2 Welch blocks, 50% overlap and Hanning windowing, corresponding to a bandwidth of 16.6 Hz (BPF 0.1).

4. Results and discussion

In this subsection, the LBM-VLES results, obtained by tripping the blade suction side at $x/c = 0.25$ and along the boundary-layer transition line location predicted by *Opty∂B*-BEMT, are presented. The numerical results are compared against the measurements carried out in the A-Tunnel of TU-Delft to assess the capability of the employed computational approach to predict the performances and aeroacoustics of low-Reynolds number propellers at engineering level. No transition trip was employed in the experimental data reported in the following. Since no acoustic data was measured at $V_\infty = 20$ m/s, due to the relatively high background noise in the experimental setup, the aeroacoustic analysis is limited to only J between 0.0 and 0.6. Hence, results for $J = 0.8$ are presented only in terms of thrust and torque coefficients. The grid independence of the numerical results was verified in a previous study carried out by the authors [16].

4.1. Mean thrust, torque and propulsive efficiency

Fig. 3 shows the comparison between the experimental and numerical thrust (C_T) and torque (C_Q) coefficients, and propulsive efficiency (η) at different advance ratios, which are computed as follows:

$$C_T = \frac{T}{\rho n^2 D^4}, \quad C_Q = \frac{Q}{\rho n^2 D^5} \quad \text{and} \quad \eta = \frac{J C_T}{2\pi C_Q}, \tag{1}$$

with T and Q being the mean propeller thrust and torque, n the number of revolutions per second and D the diameter.

As shown in Fig. 3, the thrust coefficient is predicted in a satisfactory way. The C_T is quite insensitive to the two different ways of tripping the blade suction side between $J = 0.0$ and $J = 0.6$, where the two C_T curves, obtained by tripping the blade at $x/c = 0.25$ and along the expected boundary-layer transition line, provide almost identical thrust values. Contrarily, a small difference is observed between the two numerical solutions at $J = 0.8$, as no zig-zag trip is applied on the blade suction side for the *Opty∂B*-BEMT trip case at this advance ratio (since the BEMT-trip line position completely exceeded the 80% of the chord for the entire blade span, see Fig. 2(c)). Overall, the numerical results tend to slightly underestimate the thrust generated by the propeller, except at $J = 0.8$ for the untripped numerical solution (*Opty∂B*-BEMT trip case). Although not shown for the sake of conciseness, it is observed that at $J = 0.8$ the presence of the trip causes a slightly reduction of the suction peak at the leading-edge, thus yielding to a certain thrust decrease compared to the untripped case (i.e. *Opty∂B*-BEMT). This trip effect on the pressure coefficient distribution will be briefly illustrated in Sec. 4.6, while discussing the sensitivity of the numerical results to the reduction of the trip thickness for $J = 0.0$.

Regarding the torque coefficient, the numerical predictions are in a good agreement with the experimental results for low and high values of the advance ratio, although the numerical C_Q does not show the slope sign inversion around $J = 0.24$ observed in the measurements. For intermediate J, the agreement between numerical and experimental results decreases, with the former generally showing lower values compared to the latter. A transition trip is known to provide a local increment of the skin friction across the trip itself, in addition to that associated to an earlier transition, and thus to provide some drag increment of the local airfoil section compared to an untripped case [44]. However, as previously mentioned, the trip is also responsible for a certain attenuation of the suction effect at the leading-edge in the current computations, which in turn is associated to a lower local airfoil drag generation. In addition, due to the presence of the trip, no laminar separation bubbles occur in the numerical simulations, which are known to increase the local airfoil drag [45] and thus the overall propeller torque. These aspects might represent the causes of the torque under-prediction in the numerical results despite the use of a transition trip.

Finally, the propulsive efficiency of the propeller is predicted in a very satisfactory way, except at $J = 0.8$ for the computational setup with trip at 25% of the chord. However, it should be recalled that the propulsive efficiency becomes very sensitive to even small discrepancies in the prediction of C_T and C_Q at nearly non-thrusting advance ratios, such as $J = 0.8$ in the present study, due to the relatively low values of both thrust and torque at such conditions. Interestingly, the aforementioned thrust and torque discrepancies tend to cancel out in the computation of η. The fact that thrust, torque and propulsive efficiency are weakly sensitive to the trip chordwise location highlights the industrial robustness of the proposed approach, which can be used with sufficient confidence for the sake of low-Reynolds number propeller performance prediction.

4.2. Far-field noise

Fig. 5 shows, for J between 0.0 and 0.6, the comparison between numerical and experimental far-field noise power spectral densities Φ_{aa} against the frequency f normalized by the Blade-Passing Frequency (BPF = 167 Hz). Two different microphones in the free-stream coordinate system are considered: Mic. 7 (0.0 m, 1.2 m, 0.0 m) and Mic. 11 (−0.75 m, 1.2 m, 0.0 m), respectively located in and out of the propeller plane, as depicted in Fig. 4. For each microphone and advance ratio, the unloaded (i.e. without the propeller) electric motor noise (in orange) and the background

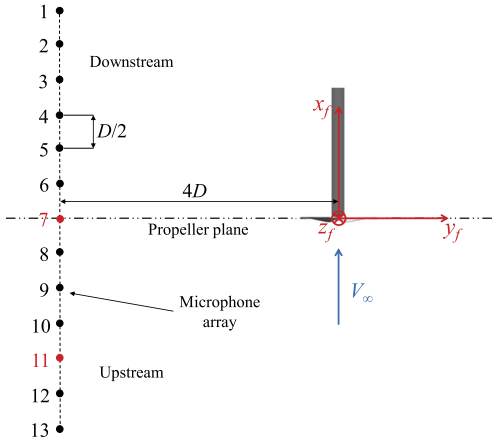

Fig. 4. Sketch of the microphone array used of far-field noise computation (drawn not to scale).

noise (in green) of the wind tunnel are reported to further support the discussion. To support the analysis of the numerical results, it is worth mentioning that the main sources of uncertainty in the experimental spectra are represented by: (i) the background noise below the wind tunnel cut-off frequency (∼200 Hz), which is responsible for the large broadband noise levels at low frequencies; (ii) the loaded electric motor noise and the non-perfect balance of the blades that cause the rise of harmonics of the shaft frequency (BPF 0.5, 1, 1.5, etc.); and (iii) the unloaded electric motor noise, which generally adds mid-frequency tonal contributions (approximately between BPF 5 to 25) to the far-field noise spectrum [16,42].

As shown in Fig. 5, the position of the transition trip on the blade suction side does not significantly affect the tonal noise component generated by propeller, even at high advance ratios where the $x/c = 0.25$ and *Opty∂B*-BEMT trip lines are distributed in a rather different way. For $J = 0.0$, the amplitude of the tone at BPF 1 is nearly the same for both the $x/c = 0.25$ and *Opty∂B*-BEMT trip cases. For increasing advance ratios, the tone at BPF 1, for the solution with trip at 25% of the chord, tends to be slightly larger than that with the BEMT trip, up to a maximum difference of about 1 dB at $J = 0.6$. This aspect is consistent with the thrust results presented in the previous section, which showed that the different trip position has a negligible impact on the thrust generation. Overall, the prediction of the BPF 1 tone is quite satisfactory compared to the measurements for all the operation conditions considered. However, while for the microphone upstream the propeller (Mic. 11), the value of the tone at BPF 1 is predicted within 1 dB difference with respect to the measurements, its prediction worsen up to an under-prediction of 3-4 dB for in-plane observer positions. Such a directional increase of the BPF 1 tone mismatch, that was also observed when comparing the measurements against BEMT-compact dipole/monopole FW-H noise computations [16], cannot be solely attributed to the lower thrust prediction observed in Fig. 3, whose impact on the radiated tonal noise is expected to be about 1.5 dB according to low-fidelity computations [16]. It might be also related to the experimental imperfect balance of the blade loading that leads to the generation of harmonics of the shaft frequency, as well as the wind-tunnel acoustic confinement effect at low frequency (i.e. test room not fully anechoic below 200 Hz).

Contrarily to the tonal component of the noise, broadband noise is more influenced by the chordwise distribution of the trip line. Since the BEMT-predicted trip lines are distributed similarly to the $x/c = 0.25$ case at low advance ratios than at high ones, it is reasonable to expect that similar boundary-layer development and turbulent boundary-layer trailing-edge noise emissions take place at low J in the numerical simulation, and that opposite situation occurs at large advance ratios. This aspect begins to be noticeable at $J = 0.4$, although it is more clearly visible at $J = 0.6$. For intermediate advance ratios ($J = 0.24 - 0.4$), the agreement between measurements and numerical solutions is fairly good. On the other hand, in hover ($J = 0.0$) and at high advance ratio ($J = 0.6$), the numerical results show a certain over-prediction and under-estimation of the broadband noise levels, respectively.

For $J = 0.0$, the larger broadband noise might be attributed to excessively high turbulent pressure fluctuations generated in the boundary-layer, promoted by the presence of a transition trip in combination with high blade loading conditions. Under such conditions, the flow experiences a higher local acceleration on the blade suction side, which would in principle require a lower trip height to initiate transition compared to higher advance ratio cases and/or more downstream trip placements, according to considerations based on the critical roughness height-based Reynolds number [44]. Hence, it is reasonable to expect that the same zig-zag trip height can lead to the development of higher turbulent fluctuations in boundary-layer under higher blade loading, as it will be qualitatively illustrated in Sec. 4.3. A sensitivity study of the numerical results to the trip thickness for $J = 0.0$ will be presented in Sec. 4.6 to further discuss, in the limit of the employed near-wall resolution, the boundary-layer over-tripping and the broadband noise over-prediction in hover.

Regarding the under-prediction of broadband noise for $J = 0.6$, it can be attributed to the absence of the laminar separation bubble and the associated acoustic feedback mechanism in the numerical solution. Such phenomena, which were observed to be the cause for the high frequency noise increment and broadband hump in the experimental data [16], are not captured in the present numerical results. This is due to the usage of a transition trip to force the turbulence model to enter into scale-resolving mode and initiate transition. However, it is worth mentioning that even in absence of the tripping device, the laminar separation bubble would be unlikely captured in the numerical solution, due to the intrinsic difficulties of the employed numerical method in capturing shallow regions of boundary-layer separation and reattachment. This aspect motivates once more the choice of using a zig-zag trip for such low-Reynolds number cases for the sake of broadband noise prediction at engineering level.

This subsection concludes the validation of the proposed computational approach, which is aimed at providing an industrial solution for the prediction of performances and tonal/broadband noise of propellers operated at low-Reynolds numbers. The following subsections provide some insights on the numerical results to further support the discussion on the effect of using a transition trip to simulate low-Reynolds number propellers, as well as the impact of its chordwise position on performances and radiated noise.

4.3. Mean and turbulent velocity fields

Figs. 6 and 7 respectively show the contours of the time-averaged velocity magnitude (V_r, expressed in the non-inertial reference frame rotating at the propeller angular velocity ω) and of the root-mean-square (V_{rms}) for the two numerical solutions obtained with trip at $x/c = 0.25$ and along the BEMT-predicted transition line for $J = 0.0 - 0.6$. The airfoil section considered is that at 70% of the blade span, which is expected to be representative of the overall aerodynamic behavior of the blade. The time-averaged velocity magnitude and the rms values are then normalized by the tip free-stream velocity experienced by the airfoil section in the body-fixed reference frame rigidly rotating with the blade, i.e. $V_{r_\infty} = \sqrt{V_\infty^2 + (\omega r)^2}$.

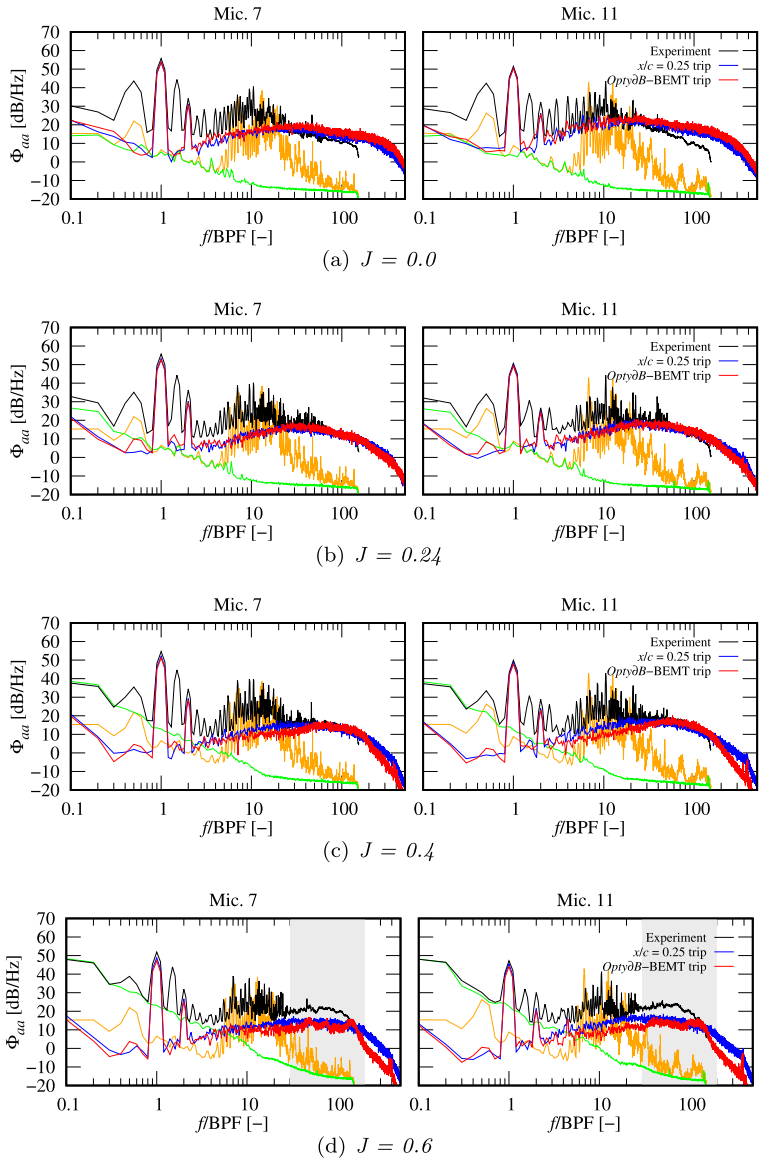

Fig. 5. Far-field noise power spectral density Φ_{aa} for in-plane (Mic. 7) and out-of-plane (Mic. 11) observer positions. Comparison between measurements and numerical solutions obtained with $x/c = 0.25$ and *Opty∂B*-BEMT trips. Unloaded electric motor noise (–) and facility background noise (–) reported for reference.

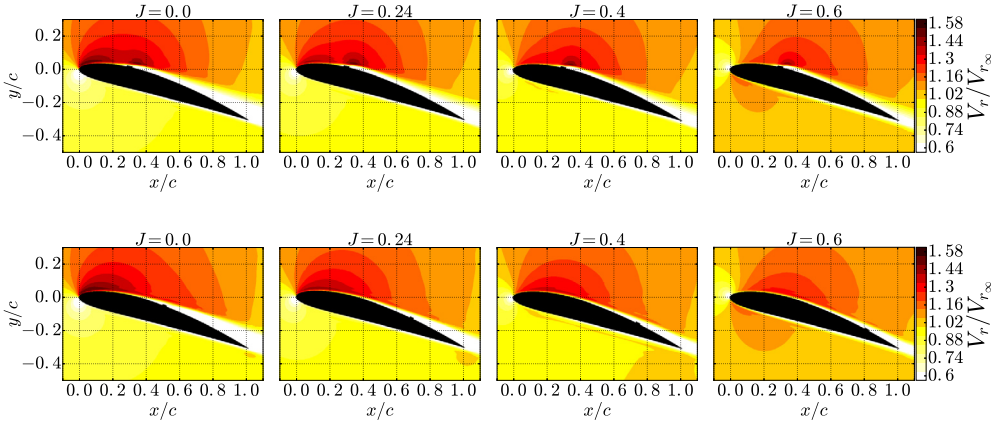

Fig. 6. Time-averaged velocity magnitude contours for the blade section at $r/R = 0.7$. Comparison between $x/c = 0.25$ (top) and *Opty∂B*-BEMT (bottom) trip computational setups.

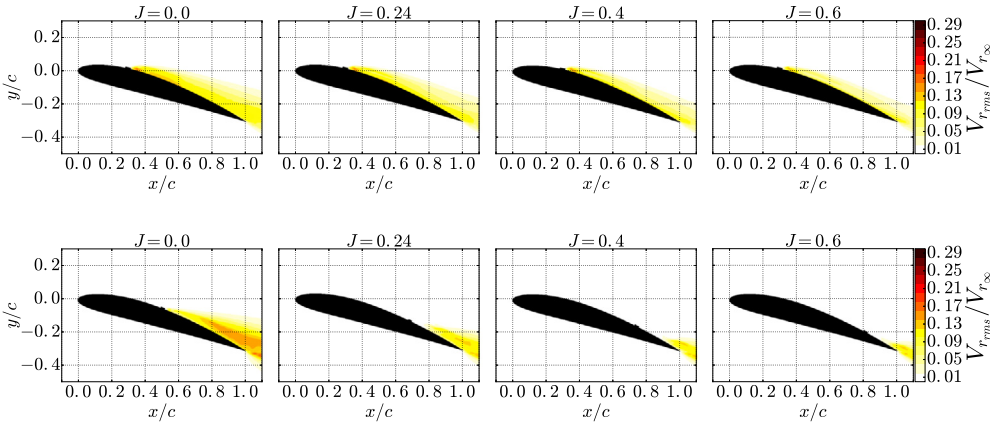

Fig. 7. Root-mean-square velocity contours for the blade section at $r/R = 0.7$. Comparison between $x/c = 0.25$ (top) and *Opty∂B*-BEMT (bottom) trip computational setups.

Interestingly, the time-averaged velocity magnitude fields (Fig. 6) show the more intrusive nature of the trip located at $x/c = 0.25$ compared to the trip distributed along the expected laminar-separation bubble reattachment line, which leads to a less pronounced flow acceleration around the blade leading-edge, a higher flow acceleration around the trip and the growth of a thicker boundary-layer downstream it. Although not reported for the sake of brevity, the inspection of the pressure coefficient distributions on the airfoil at $r/R = 0.7$ showed that the trip at 25% of the chord is responsible for a certain reduction of the suction effect at the leading-edge of the blade compared to the BEMT-predicted trip cases. However, this effect is found to be balanced out by a larger low-pressure area generated down-stream the trip, which is consistent with the rather similar C_T predictions between the two different tripping strategies observed in Fig. 3.

For all the numerical solutions with trip located at 25% of the blade chord, a similar rms velocity pattern is found, although the level of the velocity fluctuations tends to decrease as the advance ratio increases. As J increases, the local blade angle of attack and flow acceleration on the suction side decrease (Fig. 6). As a result, the same trip line experiences a slower incoming flow for increasing J and leads to the generation of lower turbulence levels in the boundary-layer downstream it (Fig. 7). Interestingly, for increasing J, the decreasing rms velocity correlates with the slightly reduction of the broadband noise shown in Fig. 5, which is associated to the scattering of the turbulent boundary-layer pressure fluctuations at the blade trailing-edge. Similarly to the cases with trip at 25% of the chord, higher advance ratio conditions correspond to a more intense velocity fluctuations in the boundary-layer also for the BEMT-predicted trip simulations. However, in such cases, the rms velocity levels decrease more rapidly as the advance ratio increases. Since the BEMT trip lines move towards the blade trailing-edge as J increases, the trip is subjected to a lower relative velocity and thicker incoming boundary-layer (as shown in Fig. 6). As a consequence, both the perturbation of the incoming flow and the generation of the fully turbulent boundary-layer by the trip are gradually mitigated for increasing J.

4.4. Wall-pressure spectrum at the trailing-edge

According to Amiet's trailing-edge noise theory [46], turbulent boundary-layer trailing-edge noise is proportional, among other quantities, to the level of wall-pressure fluctuations in proximity of the trailing-edge. Hence, the numerical wall-pressure power spectral densities Φ_{pp} on the suction side at 95% of the chord for different spanwise sections ranging between 50% and 95% of the blade radius are analyzed in this subsection (Fig. 8). It can be noted that when the blade is tripped at 25% of the chord, the boundary-layer reaches a fully-turbulent state in proximity of the trailing-edge for all the advance ratios considered, at least above $r/R = 0.5$. This can be inferred from the shape of the power spectra densities, which exhibit the typical power decay laws of a fully-developed turbulent boundary-layer, respectively proportional to $f^{-7/3}$ and f^{-5} in mid-high and very high frequency ranges [47]. In contrast, the simulations with trip line predicted by *Opty∂B*-BEMT show that a fully turbulent boundary-layer is generated only at low advance ratios ($J = 0.0 - 0.24$). For $J = 0.4$ and $J = 0.6$, only the last 30% of the blade span exhibits significant levels of wall-pressure fluctuations. These results are consistent with the rms velocity contours shown in Fig. 7 and with the broadband noise content in the far-field noise spectra shown in Fig. 5. In particular, it can be appreciated the correlation between the wall-pressure spectrum levels at the trailing-edge on the suction side and the broadband noise levels in the far-field noise computations, with the *Opty∂B*-BEMT trip case generally showing broadband noise levels higher ($J = 0.0$) or lower ($J \geq 0.4$) than those of the $x/c = 0.25$ trip case in correspondence of higher or lower resolved wall-pressure fluctuations generated at the trailing-edge, respectively. These results suggest once more the importance of using a transition trip in the present computational setup, without which not enough resolved turbulent pressure fluctuations in the boundary-layer would be generated in the numerical solution for the sake of trailing-edge noise prediction.

4.5. Beamforming noise source localization

The comparison between Clean-SC [48] beamforming noise maps on the blade suction side for the two different computational setups is shown in Fig. 10, for $J = 0.0 - 0.6$. The digital beamforming analysis is performed to ensure that the dominant source of broadband noise in the numerical results is due to turbulent boundary-layer trailing-edge noise and that spurious broadband noise sources, such as those potentially introduced by the usage of the trip, do not sensibly affect the far-field noise spectrum. The noise maps are computed from FW-H acoustic signals evaluated from a single blade on a spiral array of 226 microphones of $60R$ radius, which is defined in a reference frame rigidly rotating with the propeller for broadband noise source localization. The array, shown in Fig. 9, is centered around the propeller hub and located at $4R$ distance from it in the upstream direction. The beamforming antenna resolution at the minimum (BPF 10 = 1666 Hz) and maximum (BPF 100 = 16666 Hz) frequencies of interest is approximately equal to 30% and 3% of the mean chord, respectively. The employed Clean-SC deconvolution algorithm is implemented

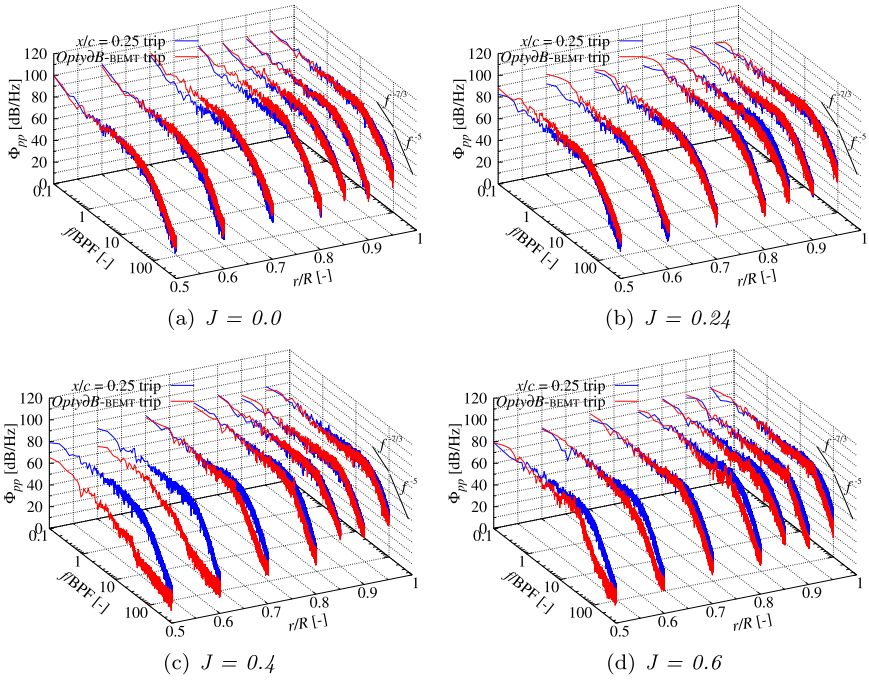

Fig. 8. Wall-pressure power spectral density Φ_{pp} on the blade suction side at $x/c = 0.95$ for different spanwise sections. Comparison between $x/c = 0.25$ and *Opty∂B*-BEMT trip computational setups.

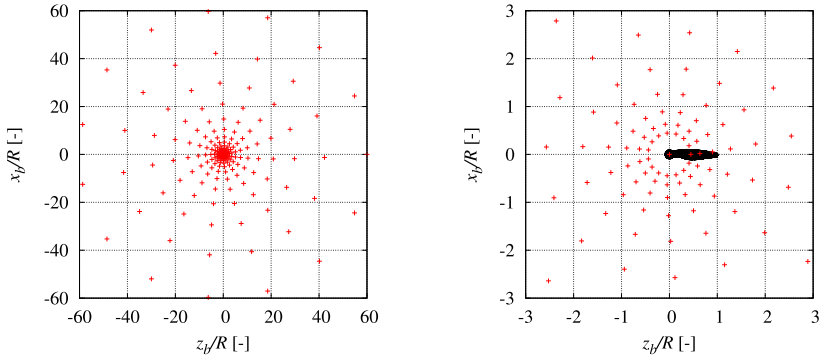

Fig. 9. Microphone array used for the beamforming noise source localization: full array (left) and array close-up view (right).

in the beamforming code *Opty∂B*-BF developed by Dassault Systèmes.

For both setups, the main broadband noise contributor between BPF 10-100 is the blade trailing-edge, through the scattering of the pressure fluctuations within the turbulent boundary-layer developing on the blade suction side, with no relevant contribution to the far-field noise clearly ascribable to the zig-zag transition trip. Both cases show that the noisiest trailing-edge region is that in proximity of the blade tip, due to higher Mach number and efficiency of the scattering process. However, while for the propeller tripped at 25% of the chord the broadband noise sources at the trailing-edge are quite uniformly distributed along the span, these are more clustered in the outer part of the blade for the BEMT-trip cases, especially as J increases. Moreover, the $x/c = 0.25$ trip configurations exhibit rather similar acoustic source images across the different advance ratios considered, with only a minor variation of their intensity and locations as J increases. The opposite situation occurs for the numerical results with trip line distribution computed by *Opty∂B*-BEMT. Overall, for all the cases examined, the beamforming noise maps magnitude variation for increasing J correlates quite well with the broadband noise reduction observed in the far-field noise spectra presented in Fig. 5. As a final remark, it is worth pointing out the presence of broadband noise sources between 80-90% of the radius on the leading-edge for the blade tripped at $x/c = 0.25$, in hover conditions. Such sources, which are not detected by the beamforming algorithm in the numerical simulations with BEMT-predicted trip, are related to the impingement of secondary turbulent structures braking down from the blade tip-vortex of the preceding blade. This breakdown phenomenon, which was observed to be more pronounced for the $x/c = 0.25$ case, is expected to be related to the occurrence of a different boundary-layer/tip-vortex interaction due to the different chordwise trip location at the tip of the blade.

4.6. Loads and noise sensitivity to trip thickness for $J = 0.0$

Fig. 5(a) showed a certain broadband noise over-prediction for $J = 0.0$ for both the trip strategies adopted, from 5 dB for observers in the propeller plane up to 10 dB for out-of-plane positions. It was conjectured that this could be related to the excessively large boundary-layer fluctuations and boundary-layer thickness promoted by a trip of 0.17 mm thickness under high blade

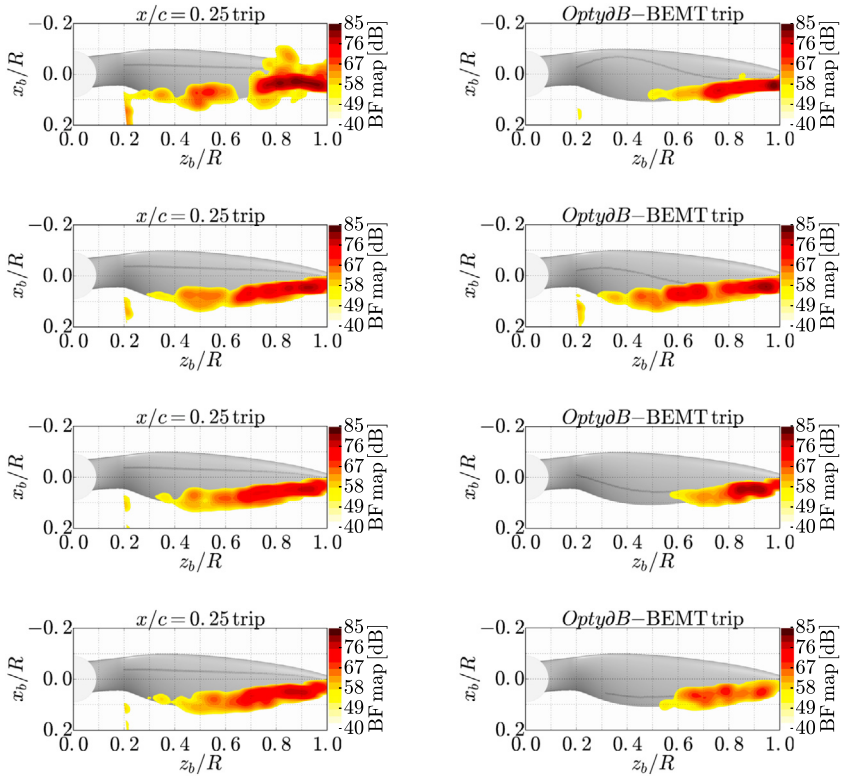

Fig. 10. Clean-SC beamforming noise maps on the blade suction side between BPF 10-100 (1666-16666 Hz) for $J = 0.0$, $J = 0.24$, $J = 0.4$ and $J = 0.6$ from top to bottom. Values below 55 dB are not shown. Comparison between $x/c = 0.25$ and *Opty∂B*-BEMT trip computational setups.

Table 1
Thrust and torque coefficients sensitivity to the trip thickness for $J = 0.0$ and trip located at $x/c = 0.25$.

Case	C_T [-]	C_T rel. err.	C_Q [-]	C_Q rel. err.
Experiment	0.117	-	0.00756	-
$x/c = 0.25$ trip (3 vox.)	0.110	−6.2%	0.00839	+10.4%
$x/c = 0.25$ trip (2 vox.)	0.113	−3.5%	0.00839	+10.4%
$x/c = 0.25$ trip (1 vox.)	0.114	−2.6%	0.00851	+11.8%

loading conditions, compared to those that would be experienced by the blade for a fully natural transitional case. Hence, a study on the sensitivity of the numerical results to the trip thickness is presented in this subsection for $J = 0.0$ and the computational setup with trip located at 25% of the chord, with the aim of shedding more light on the cause of the aforementioned discrepancies. As part of this analysis, also the sensitivity of thrust and torque to the trip height is investigated. Two additional zig-zag trips of thickness respectively equal to 0.11 mm and 0.06 mm (corresponding to a height of 2 voxels and 1 voxel, respectively), are considered in addition to the trip of 0.17 mm (3 voxels) that was considered in the previous subsections. It is worth recalling that the 0.06 mm trip thickness (corresponding to 1 finest voxel) represents the lowest trip height that can be achieved with the current computational grid.

Table 1 reports the variation of the thrust and torque coefficients with respect to the trip height. It can be observed that the reduction of the trip thickness leads to an improvement of the C_T prediction, from a under-estimation of −6% for the thicker trip, to an under-prediction of about −3% for the thinner one. Conversely, the torque coefficient shows a lower sensitivity to the trip height, with a minor over-prediction increment by 1%, most likely consequence of the increased induced drag due to the increased lift distribution generated along the span.

Fig. 11 depicts the pressure coefficient, time-averaged velocity magnitude and root-mean-square contours for the blade section at 70% of the radial coordinate. As for the time-averaged velocity magnitude and root-mean-square, also the C_p is normalized considering the dynamic pressure based on the local free-stream velocity experienced by the airfoil. The pressure coefficient contours show that a larger low-pressure area is generated around the blade leading-edge on the suction side as the trip height is reduced. At the same time, the region downstream the trip is characterized by a slower recovery of the free-stream pressure for the smaller trip height. These aspects are consistent with the larger thrust generation observed in Table 1. The C_p contours also show the trivial consideration that a thinner trip exerts a less intrusive action on the surrounding flow. This aspect is also clearly noticeable from the time-averaged velocity magnitude contours, which further illustrates that a progressively lower flow acceleration is established around the trip as the trip height is reduced. Furthermore, a reduced trip thickness leads to the generation of a higher flow acceleration around the blade leading-edge, which is consistent with the increment of the pressure suction effect described above. Concerning the root-mean-square of the velocity, the trip thickness is seen to play a major role on the turbulent development right downstream the trip (i.e. bypass transition process [49]) rather than on the ultimate levels of fluctuations that are achieved in proximity of the blade trailing-edge.

Finally, Fig. 12 shows the far-field noise sound pressure level $L_{p(1/3)}$ plotted in 1/3-octave frequency bands to better discern high-frequency broadband noise variations for the three different trip heights considered. The two microphone positions are the same as in Sec. 4.2. Similarly to what has been previously observed regarding the trip chordwise position, it can be noted that also trip thickness has no influence on the tonal component of the noise, at least for the three trip heights analyzed in this study, for which no flow separation is induced by the trip itself. Moreover, also the

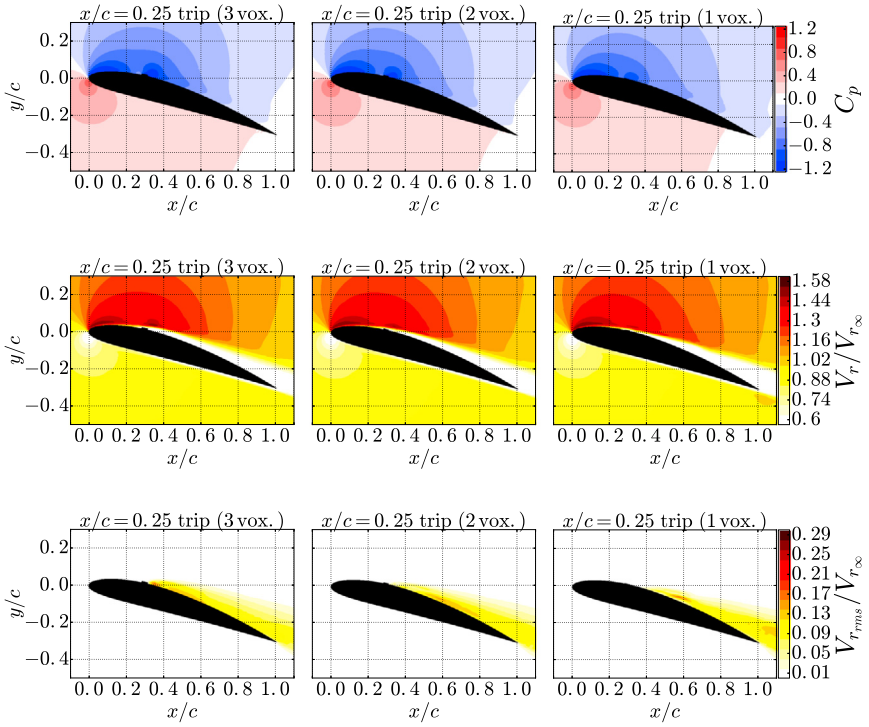

Fig. 11. Pressure coefficient (top), time-averaged velocity magnitude (center) and root-mean-square velocity (bottom) contours for the blade section at $r/R = 0.7$. Comparison between three trip thicknesses for the computational setup with trip at $x/c = 0.25$.

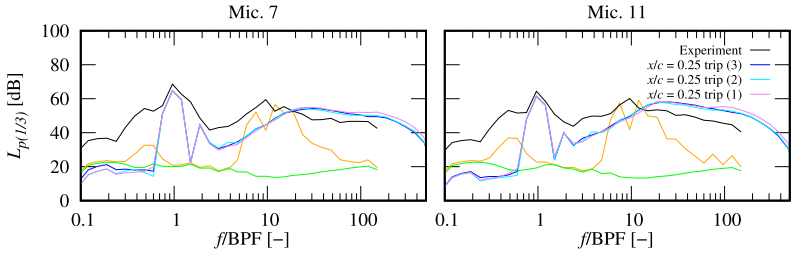

Fig. 12. Sound pressure level in 1/3-octave band $L_{p(1/3)}$ for in-plane (Mic. 7) and out-of-plane (Mic. 11) observer positions. Comparison between measurements and numerical solutions obtained with $x/c = 0.25$ and three different trip thicknesses. Unloaded electric motor noise (–) and wind tunnel background noise (–) reported for reference.

broadband component of the noise shows a very minor sensitivity to the three trip thicknesses considered, for a zig-zag trip placed at 25% of the chord and under hover conditions. Although this aspect is to some extent surprising, it could have been expected based on the root-mean-square velocity contours shown in Fig. 11, which qualitatively showed comparable turbulence levels in proximity of the trailing-edge, thus suggesting similar turbulent boundary-layer trailing-edge noise radiations. Surprisingly, the smallest trip height generates slightly higher broadband noise emissions for frequencies above BPF 100 compared to the two other trip thicknesses. This might be the consequence of smaller scales of turbulence being triggered by a smaller trip within the transition process taking place downstream it.

Fig. 12 shows that for the two additional trip heights of 0.11 mm and 0.05 mm broadband noise is also over-estimated from 5 to 10 dB for $J = 0.0$. For three-dimensional tripping devices, Van Rooij and Timmer [50] proposed a critical roughness height-based Reynolds number $Re_k = 200$ (where $Re_k = uk/\nu$, with u being the local flow velocity and ν the kinematic viscosity) to define a minimum trip thickness k to trigger transition. Based on this criterion, and considering a local velocity of the flow approaching the trip $u \approx 1.4 V_{r_\infty}$ (see Fig. 11) a critical trip thickness of approximately 0.04 mm can be determined for $r/R = 0.70$ for initiating transition in hover. With this regard, all the three trip thickness considered would lead to an over-tripped boundary-layer above 70% of the blade span, which might explain the origin of the broadband noise over-prediction for $J = 0.0$. Nevertheless, the low sensitivity of loads and broadband noise radiation to the trip thickness, in addition to that to the trip chordwise position discussed above, plays in favor of the robustness of the proposed approach for industrial applications.

5. Conclusions

This paper presented a computational approach based on the LB/VLES method to predict the performances and noise signature associated to a two-bladed propeller operated at low Reynolds numbers. The numerical flow solution was obtained by solving the explicit, transient and compressible lattice-Boltzmann equation implemented in the CFD/CAA solver SIMULIA PowerFLOW®. The aerodynamic noise generated by the propeller was computed by using an acoustic analogy based on Farassat's formulation 1A of the FW-H equation applied to the propeller/nacelle surfaces. A transition trip was included in the computational setup to force the numerical scheme to switch from modeled to scale-resolving turbulence, and to trigger the formation of vortical structures with

scales able to emulate the complexity of the low-Reynolds number boundary-layer on the blade. Two different tripping strategies were attempted by positioning the trip along the quarter-chord and the expected turbulent boundary-layer transition lines, respectively.

Numerical results were compared against loads and noise measurements carried out in the A-Tunnel of TU-Delft. Overall, thrust and torque predictions were found to be in a satisfactory agreement with respect to the experimental results, although some discrepancies were observed for the former at low and middle advance ratios, and at intermediate ones for the latter. The trip position marginally affected the thrust, and to a slightly greater extent the torque predictions. Both tonal and broadband prediction compared favorably against the experimental data, especially for intermediate advance ratios. A certain over-prediction of the broadband noise levels were found for the hover case, due to excessively high levels of turbulence generated by the trip under high blade loading conditions. Contrarily, at $J = 0.6$ the numerical results did not show the measured high-frequency broadband hump associated to laminar bubble separation noise, with both the computational setups predicting lower broadband noise. Tonal noise did not show a significant sensitivity to the trip chordwise position, whereas broadband noise levels were found to be affected to a slightly larger extent by the chordwise position of the trip.

A further investigation of the rms velocity fields and wall-pressure spectra at the trailing-edge on the blade suction side revealed that the formation of a fully-turbulent boundary-layer is achieved for most of the blade span for the blade tripped at 25% of the chord. Contrarily, the simulations with trip derived from BEMT calculations exhibited a lower spanwise extension of high turbulent activity regions as the advance ratio increases. These results were confirmed by Clean-SC beamforming noise maps calculations, which showed that broadband noise sources generated at the trailing-edge are more uniformly distributed along the span for the propeller tripped at 25% of the chord, in contrast to the BEMT-trip cases, especially for increasing advance ratios. The beamforming results further showed that the trip did not contribute in a tangible way to the broadband noise levels.

The satisfactory agreement of thrust, torque and tonal/broadband noise numerical results with respect to the experimental measurements validated the proposed approach for the prediction of performances and noise radiation associated to low-Reynolds number propellers at engineering level. Moreover, the robustness of the proposed method for industrial studies was corroborated by the low sensitivity of the trip chordwise location and height. As future outlook, simulations with spanwise varying trip thickness, based on a critical roughness height-based Reynolds number, and local mesh refinement around the trip geometry will be performed to improve the broadband noise prediction in hover ($J = 0.0$). Moreover, untripped implicit LB/VLES simulations, in which the inviscid energy cascade through the inertial range is captured by the numerical scheme and the inherent numerical dissipation acts as sub-grid model, will be attempted with the scope of capturing the laminar separation bubble, the consequent boundary-layer behavior and the associated noise radiation featuring propellers operating at low-Reynolds numbers.

Declaration of competing interest

The authors declare that they have no known competing financial interests or personal relationships that could have appeared to influence the work reported in this paper.

References

[1] G. Sinibaldi, L. Marino, Experimental analysis on the noise of propellers for small uav, Appl. Acoust. 74 (1) (2013) 79–88, https://doi.org/10.1016/j.apacoust.2012.06.011.

[2] N.S. Zawodny, D.D. Boyd Jr, C.L. Burley, Acoustic characterization and prediction of representative, small-scale rotary-wing unmanned aircraft system components, Tech. Rep. NF1676L-22587, NASA, 2016.

[3] Y. Yang, Y. Liu, Y. Li, E. Arcondoulis, Y. Wang, Aerodynamic and aeroacoustic performance of an isolated multicopter rotor during forward flight, AIAA J. 58 (3) (2020) 1171–1181, https://doi.org/10.2514/1.J058459.

[4] C. Thurman, N.S. Zawodny, N.A. Pettingill, L.V. Lopes, J.D. Baeder, Physics-informed broadband noise source identification and prediction of an ideally twisted rotor, in: AIAA SciTech 2021 Forum, 2021, p. 1925, https://doi.org/10.2514/6.2021-1925.

[5] R.R. Mankbadi, S.O. Afari, V.V. Golubev, High-fidelity simulations of noise generation in a propeller-driven unmanned aerial vehicle, AIAA J. 59 (3) (2021) 1020–1039, https://doi.org/10.2514/1.J059117.

[6] J. Holden, N. Goel, Fast-Forwarding to a Future of on-Demand Urban Air Transportation, Uber Elevate - White Paper, 2016.

[7] S. Rizzi, D.L. Huff, B.S. Henderson, P. Bent, K.A. Pascioni, D.C. Sargent, D.L. Josephson, M. Marsan, H. He, R. Snider, Urban air mobility noise: Current practice, gaps, and recommendations, NASA/TP–2020-50074337, 2020.

[8] S. Glegg, W. Devenport, Aeroacoustics of Low Mach Number Flows: Fundamentals, Analysis, and Measurement, Academic Press, 2017.

[9] M.S. Boutilier, S. Yarusevych, Parametric study of separation and transition characteristics over an airfoil at low Reynolds numbers, Exp. Fluids 52 (6) (2012) 1491–1506, https://doi.org/10.1007/s00348-012-1270-z.

[10] S. Pröbsting, S. Yarusevych, Laminar separation bubble development on an airfoil emitting tonal noise, J. Fluid Mech. 780 (2015) 167, https://doi.org/10.1017/jfm.2015.427.

[11] J. Brandt, M. Selig, Propeller performance data at low Reynolds numbers, in: 49th AIAA Aerospace Sciences Meeting Including the New Horizons Forum and Aerospace Exposition, 2011, p. 1255, https://doi.org/10.2514/6.2011-1255.

[12] A. Leslie, K. Wong, D. Auld, Broadband noise reduction from a mini-uav propeller through boundary layer tripping, in: 14th AIAA/CEAS Aeroacoustics Conference, 2008, https://doi.org/10.2514/6.2008-3069.

[13] J. Winslow, H. Otsuka, B. Govindarajan, I. Chopra, Basic understanding of airfoil characteristics at low Reynolds numbers ($10^4 - 10^5$), J. Aircr. 55 (3) (2018) 1050–1061, https://doi.org/10.2514/1.C034415.

[14] G. Yakhina, M. Roger, S. Moreau, L. Nguyen, V. Golubev, Experimental and analytical investigation of the tonal trailing-edge noise radiated by low Reynolds number aerofoils, in: Acoustics, vol. 2, Multidisciplinary Digital Publishing Institute, 2020, pp. 293–329, https://doi.org/10.3390/acoustics2020018.

[15] E.J.G. Arcondoulis, C.J. Doolan, A.C. Zander, L.A. Brooks, A review of trailing edge noise generated by airfoils at low to moderate Reynolds number, Acoust. Aust. 38 (3) (2010).

[16] D. Casalino, E. Grande, G. Romani, D. Ragni, F. Avallone, Definition of a benchmark for low Reynolds number propeller aeroacoustics, Aerosp. Sci. Technol. 113 (2021) 106707, https://doi.org/10.1016/j.ast.2021.106707.

[17] D. Casalino, M. Barbarino, A. Visingardi, Simulation of helicopter community noise in complex urban geometry, AIAA J. 49 (8) (2011) 1614–1624, https://doi.org/10.2514/1.J050774.

[18] C. Wagner, T. Hüttl, P. Sagaut, Large-Eddy Simulation for Acoustics, vol. 20, Cambridge University Press, 2007, https://doi.org/10.1017/CBO9780511546143.

[19] G. Romani, D. Casalino, Rotorcraft blade-vortex interaction noise prediction using the Lattice-Boltzmann method, Aerosp. Sci. Technol. 88 (2019) 147–157, https://doi.org/10.1016/j.ast.2019.03.029.

[20] G. Romani, Q. Ye, F. Avallone, D. Ragni, D. Casalino, Numerical analysis of fan noise for the nova boundary-layer ingestion configuration, Aerosp. Sci. Technol. 96 (2020) 105532, https://doi.org/10.1016/j.ast.2019.105532.

[21] C. Mockett, W. Haase, D. Schwamborn, Go4Hybrid: Grey Area Mitigation for Hybrid RANS-LES Methods, vol. 134, Springer, 2018, https://doi.org/10.1007/978-3-319-52995-0.

[22] F. Menter, J. Schutze, K. Kurbatskii, R. Lechner, M. Gritskevich, A. Garbaruk, Scale-resolving simulation techniques in industrial cfd, in: 6th AIAA Theoretical Fluid Mechanics Conference, 2011, p. 3474, https://doi.org/10.2514/6.2011-3474.

[23] V. Yakhot, S.A. Orszag, Renormalization group analysis of turbulence. I. Basic theory, J. Sci. Comput. 1 (1) (1986) 3–51, https://doi.org/10.1007/BF01061452.

[24] V. Yakhot, S.A. Orszag, S. Thangam, T.B. Gatski, C.G. Speziale, Development of turbulence models for shear flows by a double expansion technique, Phys. Fluids A 4 (7) (1992) 1510–1520, https://doi.org/10.1063/1.858424.

[25] H. Chen, S. Kandasamy, S.A. Orszag, S. Succi, V. Yakhot, Extended Boltzmann kinetic equation for turbulent flows, Science 301 (5633) (2003) 633–636, https://doi.org/10.1126/science.1085048.

[26] H. Chen, S. Orszag, I. Staroselsky, S. Succi, Expanded analogy between Boltzmann kinetic theory of fluid and turbulence, J. Fluid Mech. 519 (2004) 301–314, https://doi.org/10.1017/S0022112004001211.

[27] X. Shan, X.-F. Yuan, H. Chen, Kinetic theory representation of hydrodynamics: a way beyond the Navier-Stokes equation, J. Fluid Mech. 550 (2006) 413, https://doi.org/10.1017/S0022112005008153.

[28] R. Zhang, X. Shan, H. Chen, Efficient kinetic method for fluid simulation beyond the Navier-Stokes equation, Phys. Rev. E 74 (4) (2006) 046703, https://doi.org/10.1103/PhysRevE.74.046703.

[29] H. Chen, I. Goldhirsch, S.A. Orszag, Discrete rotational symmetry, moment isotropy, and higher order lattice Boltzmann models, J. Sci. Comput. 34 (1) (2008) 87–112, https://doi.org/10.1007/s10915-007-9159-3.
[30] H. Chen, R. Zhang, P. Gopalakrishnan, Filtered lattice Boltzmann collision formulation enforcing isotropy and Galilean invariance, Phys. Scr. 95 (3) (2020) 034003, https://doi.org/10.1088/1402-4896/ab4b4d.
[31] H. Chen, S. Chen, W. Matthaeus, Recovery of the Navier-Stokes equations using a lattice-gas Boltzmann method, Phys. Rev. A 45 (8) (1992) 5339–5342, https://doi.org/10.1103/PhysRevA.45.R5339.
[32] P.L. Bhatnagar, E.P. Gross, M. Krook, A model for collision processes in gases. I. Small amplitude processes in charged and neutral one-component systems, Phys. Rev. 94 (3) (1954) 511–525, https://doi.org/10.1103/PhysRev.94.511.
[33] H. Chen, C. Teixeira, K. Molvig, Realization of fluid boundary conditions via discrete Boltzmann dynamics, Int. J. Mod. Phys. C 9 (8) (1998) 1281–1292, https://doi.org/10.1142/S0129183198001151.
[34] R. Zhang, C. Sun, Y. Li, R. Satti, R. Shock, J. Hoch, H. Chen, Lattice Boltzmann approach for local reference frames, Commun. Comput. Phys. 9 (5) (2011) 1193–1205, https://doi.org/10.4208/cicp.021109.111110s.
[35] G. Tabor, A.D. Gosman, R.I. Issa, Numerical simulation of the flow in a mixing vessel stirred by a Rushton turbine, in: Institution of Chemical Engineers Symposium Series, vol. 140, Citeseer, 1996, pp. 25–34.
[36] J.E. Ffowcs Williams, D.L. Hawkings, Sound generated by turbulence and surfaces in arbitrary motion, Philos. Trans. R. Soc. Lond. Ser. A 264 (1151) (1969) 321–342, https://doi.org/10.1098/rsta.1969.0031.
[37] D. Casalino, An advanced time approach for acoustic analogy predictions, J. Sound Vib. 261 (4) (2003) 583–612, https://doi.org/10.1016/S0022-460X(02)00986-0.
[38] F. Farassat, G.P. Succi, The prediction of helicopter discrete frequency noise, Vertica 7 (4) (1983) 309–320.
[39] J.E. Ffowcs Williams, L.H. Hall, Aerodynamic sound generation by turbulent flow in the vicinity of a scattering half-plane, J. Fluid Mech. 40 (1970) 657–670, https://doi.org/10.1017/S0022112070000368.
[40] N. Curle, The influence of solid boundaries upon aerodynamic sound, Proc. R. Soc. Lond. A 231 (1955) 505–514, https://doi.org/10.1098/rspa.1955.0191.
[41] M.J. Lighthill, On sound generated aerodynamically: 1. General theory, Proc. R. Soc. Lond. A 211 (1107) (1952) 564–578, https://doi.org/10.1098/rspa.1952.0060.
[42] E. Grande, G. Romani, D. Ragni, F. Avallone, D. Casalino, Aeroacoustic investigation of a propeller operating at low-Reynolds number, AIAA J. (2021), in press.
[43] G. Elsinga, J. Westerweel, Tomographic-piv measurement of the flow around a zigzag boundary layer trip, Exp. Fluids 52 (4) (2012) 865–876, https://doi.org/10.1007/s00348-011-1153-8.
[44] A.L. Braslow, Simplified Method for Determination of Critical Height of Distributed Roughness for Boundary-layer Transition at Mach Numbers from 0 to 5, no. TN-4363, National Advisory Committee for Aeronautics, 1958.
[45] W. Zhang, R. Hain, C.J. Kähler, Scanning piv investigation of the laminar separation bubble on a sd7003 airfoil, Exp. Fluids 45 (4) (2008) 725–743, https://doi.org/10.1007/s00348-008-0563-8.
[46] R.K. Amiet, Noise due to turbulent flow past a trailing edge, J. Sound Vib. 47 (3) (1976) 387–393, https://doi.org/10.1016/0022-460X(76)90948-2.
[47] W.K. Blake, Mechanics of Flow-Induced Sound and Vibration, Academic Press, 1986.
[48] P. Sijtsma, Clean based on spatial source coherence, Int. J. Aeroacoust. 6 (4) (2007) 357–374, https://doi.org/10.1260/147547207783359459.
[49] E. Reshotko, Transition issues for atmospheric entry, J. Spacecr. Rockets 45 (2) (2008) 161–164, https://doi.org/10.2514/1.29777.
[50] R. Van Rooij, W. Timmer, Roughness sensitivity considerations for thick rotor blade airfoils, J. Sol. Energy Eng. 125 (4) (2003) 468–478, https://doi.org/10.1115/1.1624614.